

A 3D Wideband GBSM for THz Communications in Indoor Scenarios

Yiling Huang¹, Hengtai Chang¹, Jie Huang^{2,3}, Wensheng Zhang¹, Jian Sun¹, and Cheng-Xiang Wang^{2,3}

¹Shandong Provincial Key Lab of Wireless Communication Technologies, School of Information Science and Engineering, Shandong University, Qingdao 266237, China.

²National Mobile Communications Research Laboratory, School of Information Science and Engineering, Southeast University, Nanjing 210096, China.

³Purple Mountain Laboratories, Nanjing 211111, China

Email: huangyl0408@163.com, hunter_chang@126.com, j_huang@seu.edu.cn, zhangwsh@sdu.edu.cn, sunjian@sdu.edu.cn, chxwang@seu.edu.cn

Abstract—In this paper, we propose a three-dimensional (3D) wideband reference regular-shaped geometry-based stochastic model (RS-GBSM) at terahertz (THz) bands for indoor scenarios. The corresponding sum-of-sinusoid (SoS) simulation model is established to verify the reference model. The proposed model combines a two-sphere model with an elliptic cylinder model, where the received signal is considered as a summation of the line-of-sight (LoS), single-bounce (SB), and double-bounce (DB) components. The von-Mises-Fisher (VMF) distribution is applied to the expressions of azimuth and elevation angles to depict the distribution of scatterers. Based on the proposed THz RS-GBSM, the power delay profile (PDP) and channel transfer function (CTF) are obtained. The delay spread and frequency correlation function (FCF) are investigated. The simulation results demonstrate the validity of the proposed model to describe indoor THz channels.

Index Terms—THz channel modeling, GBSM, power delay profile, channel transfer function, frequency correlation function

I. INTRODUCTION

With the rapid developments of Internet of things (IoT), more and more smart devices are accessed to wireless communication networks. The demand of larger capacity and higher data rate is becoming urgent for daily consumption and entertainment. Tens of Gbps links will be required to meet the huge demand of mobile traffic [1]. Evidently, larger bandwidth and more spectrum resource should be applied to satisfy the future high-speed transmission. As the fifth generation (5G) wireless communication is being commercially used, the research on millimeter-wave communications is sufficient [2]–[5]. THz band is explored to confront the limitation of the spectrum and the ever-growing trend. THz communication is now considered as one of the key technologies for the sixth generation (6G) wireless communications.

Generally, the THz band is from 0.1 THz to 10 THz, and international telecommunication union (ITU) defines the THz band as from 300 GHz to 3 THz. THz communications can provide more than 20 GHz bandwidth and achieve Tbps data rate [6], which coincides with the communication desire. Due to the short wavelength of THz wave, which is less than 1 mm, the antennas equipped to the THz devices can be more miniaturized. Besides, THz wave will be attenuated when

penetrating non-transparent objects, and absorbed by water vapour and oxygen molecules. Therefore, appropriate frequency windows should be chosen to mitigate the absorption and high directional antennas are needed to compensate such high attenuation and provide more confidential and anti-interference communication.

Several THz communication scenarios have been defined in the IEEE 802.15.3d standard, including the close proximity peer-to-peer (P2P), data center networks, intra-device communication, wireless backhaul, and wireless fronthaul [7]. In addition, researchers also carried on some work about wireless local area network (WLAN) and nano cell scenarios [8], [9]. Kiosk downloading [10], [11], as a kind of close proximity P2P applications, supports comparatively short-range (<1 m) communication between the kiosk downloading and the smart phones or other electronic devices. In [10] and [11], the authors used the non-GBSM (NGBSM) at 300 GHz to investigate the kiosk downloading channel characteristics and compared the results with the measurement data. The intra-device application is chip-to-chip communication, which aims to reduce the number of pins. The parameters of full bandwidth from 270 GHz to 320 GHz and three sub-bands were analyzed [7], [12]. THz wave applying to data center scenario can replace the wire link that will cut down the maintenance cost and promote space efficiency. In [13], ray tracing was used to calibrate the channel model for 300 GHz data center scenario and improve the conformity and accuracy. In backhaul/fronthaul scenarios, large-scale fading was considered, including atmospheric gas attenuation, cloud, fog, and rain attenuation [7]. In [14] and [15], a two-dimensional (2D) concentric sectors GBSM was proposed for short-range device-to-device (D2D) wideband THz channels with directional antennas both at the transmitter (Tx) and receiver (Rx) sides. In [16] and [17], the authors proposed NGBSM in typical office scenarios and carried out measurements to calibrate the ray tracing model so that the channel models could be validated by the measurements. Other measurements were also conducted to investigate the properties of THz channels in [18]–[20].

In general, plenty of researches have been done both on THz channel modeling and measurements and focused on the

frequency band around 300 GHz. However, there is not enough work about GBSMs at THz bands. For a GBSM, there is no need to know all the parameters of the propagation environment. It uses certain probability density functions (PDFs) to describe the locations of the scatterers and therefore, it is more general and more flexible. GBSMs have been proposed for, e.g., millimeter-wave communications, optical wireless communications, and other 5G channels [4], [21]–[25]. What's more, as the propagation distance of the THz wave is short, it is more precise to adopt a 3D model to describe the indoor THz channels. To the best of our knowledge, it is the first time to propose a 3D wideband GBSM for THz channels. The proposed RS-GBSM combines a two-sphere model with an elliptical cylinder model for indoor channels at 300 GHz as the existing measurements are mostly around 300 GHz. In the model, we consider both the LoS path and the non-LoS (NLoS) paths, including SB and DB components, because of the little contribution of higher order bounces. For actual measurement, rotating antenna was applied to traverse each direction [26]. In order to facilitate the verification of our model, the Tx and Rx are both equipped with omnidirectional antennas. Besides, the model can also be applied to directional antennas. Based on the calculated channel impulse response (CIR), we can further obtain the PDP, delay spread, and CTF, and then compare all these results with measurement data to validate the feasibility of the proposed model, especially the evident effect of the top surface of the elliptical cylinder. Moreover, the channel characteristics in frequency domain in accordance with the FCF are analyzed.

The remainder of this paper is organized as follows. Section II describes the proposed RS-GBSM in details. In Section III, channel characteristics are calculated and analyzed. In Section IV, the results of reference model, simulation model, simulation and measurement results are compared. Finally, conclusions are drawn in Section V.

II. A THz RS-GBSM

The proposed THz RS-GBSM is shown in Fig. 1. It's similar to the vehicle-to-vehicle (V2V) RS-GBSM in [27].

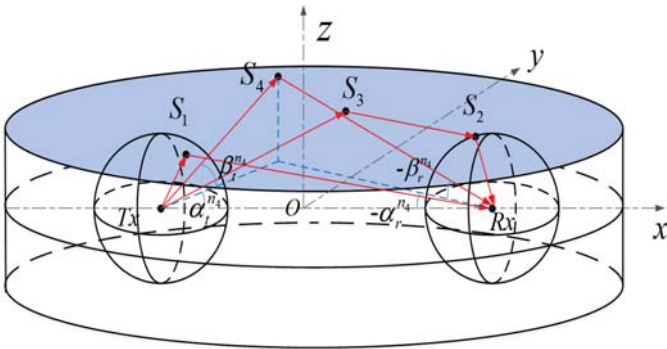


Fig. 1. A 3D GBSM for THz channels.

TABLE I
MULTIPATHS CONSIDERED IN THE MODEL.

Component	Path	Distance
LoS	$Tx-Rx$	d_{LoS}
SB	$Tx-S_1-Rx$	$d_{n_1} = d_{TxS_1} + d_{S_1Rx}$
	$Tx-S_2-Rx$	$d_{n_2} = d_{TxS_2} + d_{S_2Rx}$
	$Tx-S_3-Rx$	$d_{n_3} = d_{TxS_3} + d_{S_3Rx}$
	$Tx-S_4-Rx$	$d_{n_4} = d_{TxS_4} + d_{S_4Rx}$
DB	$Tx-S_1-S_2-Rx$	$d_{n_1n_2} = d_{TxS_1} + d_{S_1S_2} + d_{S_2Rx}$
	$Tx-S_1-S_3-Rx$	$d_{n_1n_3} = d_{TxS_1} + d_{S_1S_3} + d_{S_3Rx}$
	$Tx-S_1-S_4-Rx$	$d_{n_1n_4} = d_{TxS_1} + d_{S_1S_4} + d_{S_4Rx}$
	$Tx-S_3-S_2-Rx$	$d_{n_3n_2} = d_{TxS_3} + d_{S_3S_2} + d_{S_2Rx}$
	$Tx-S_4-S_2-Rx$	$d_{n_4n_2} = d_{TxS_4} + d_{S_4S_2} + d_{S_2Rx}$

The difference is that we add the top surface of the elliptical cylinder to model the ceiling of the room. Therefore, it can better describe the indoor scenarios and the indispensability of the top surface will be shown in Section IV. As the floor is always covered by objects, we don't consider the effects of the bottom surface. The two spheres and the side of the elliptical cylinder describe the scatterers around the Tx, the Rx, and on the wall, respectively.

Let us assume that there are N_1 scatterers laying on the sphere at the Tx side, denoted by S_1 , and N_2 scatterers laying on the sphere at the Rx side, denoted by S_2 . There are N_3 scatterers on the side of the elliptical cylinder, denoted by S_3 , and N_4 scatterers on the top surface of the elliptical cylinder, denoted by S_4 . The Tx and Rx are set on the focuses of the ellipse which is the cross section of the elliptical cylinder. We establish a 3D coordinate system with the midpoints of the two focuses as the origin and assume the coordinate of scatterer S_l is $S_l(x_l, y_l, z_l)$.

A. Reference model

The proposed model contains the LoS component, SB paths, and part of DB paths. The specific multipaths are shown in Table I. The definition of parameters are shown in Table II. For the reference model, we assume that the numbers of all the scatterers are infinite, i.e., $N_1, N_2, N_3, N_4 \rightarrow \infty$.

The CIR can be expressed as a summation of the three components mentioned above, i.e.,

$$h(\tau) = h_{LoS}(\tau) + h_{SB}(\tau) + h_{DB}(\tau). \quad (1)$$

The LoS component of the CIR is given as

$$h_{LoS}(\tau) = \sqrt{\frac{K}{K+1}} e^{-j2\pi f_c \tau_{LoS}} \delta(\tau - \tau_{LoS}) \quad (2)$$

where λ is the wavelength, $f_c = 300$ GHz is the carrier frequency, $\tau_{LoS} = d_{LoS}/c$ is the delay of the LoS link, $d_{LoS} = D$ is the distance between the Tx and Rx, c is the speed of light, and K is the Ricean factor representing the ratio of the LoS power and the scattered power.

TABLE II
DEFINITION OF PARAMETERS.

Parameter	Definition
D	Distance between the Tx and the Rx
a	Semi-major axis of the elliptic cylinder
R_t, R_r	Radius of the Tx and the Rx spheres, respectively
$\alpha_t^{n_l}, \alpha_r^{n_l}$	Azimuth angles of departure (AAoD) and arrival (AAoA) of scatterer S_l , respectively, $\alpha_t^{n_l}, \alpha_r^{n_l} \in [-\pi, \pi]$
$\beta_t^{n_l}, \beta_r^{n_l}$	Elevation angles of departure (EAoD) and arrival (EAoA) of scatterer S_l , respectively, $\beta_t^{n_l}, \beta_r^{n_l} \in [-\pi, \pi]$
$\alpha_{t0}, \beta_{t0}, \alpha_{r0}, \beta_{r0}$	Mean values of $\alpha_t^{n_l}, \beta_t^{n_l}, \alpha_r^{n_l}$, and $\beta_r^{n_l}$, respectively
$\varphi_{n_l}, \varphi_{n_l n_m}$	Phases of the SB path $Tx-S_l-Rx$ and the DB path $Tx-S_l-S_m-Rx$, respectively, $\varphi_{n_l}, \varphi_{n_l n_m} \in [0, 2\pi)$

The SB component of the CIR can be expressed as

$$h_{SB}(\tau) = \sqrt{\frac{\eta_{SB}}{K+1}} \frac{1}{\sqrt{L}} \sum_{l=1}^L \lim_{N_l \rightarrow \infty} \frac{1}{\sqrt{N_l}} \sum_{n_l=1}^{N_l} e^{j\varphi_{n_l} - j2\pi f_c \tau_{n_l}} \delta(\tau - \tau_{n_l}) \quad (3)$$

where η_{SB} is the proportion of the SB power in the NLoS power, $L = 4$ is the number of the species of the SB scatterers, N_l is the number of scatterers S_l . Here, $\tau_{n_l} = d_{n_l}/c$ is the delay of path $Tx-S_l-Rx$. The distance of each path ε_{n_l} can be seen as the superposition of the length of the segments with Tx/Rx and S_l as endpoints, i.e.,

$$d_{n_l} = \sqrt{(x_l + D/2)^2 + y_l^2 + z_l^2} + \sqrt{(x_l - D/2)^2 + y_l^2 + z_l^2}. \quad (4)$$

The DB component of the CIR is expressed as

$$h_{DB}(\tau) = \sqrt{\frac{\eta_{DB}}{K+1}} \frac{1}{\sqrt{LM}} \sum_{l=1}^L \sum_{m=1}^M \lim_{N_l \rightarrow \infty} \lim_{N_m \rightarrow \infty} \frac{1}{\sqrt{N_l N_m}} \sum_{n_l=1}^{N_l} \sum_{n_m=1}^{N_m} e^{j\varphi_{n_l n_m} - j2\pi f_c \tau_{n_l n_m}} \delta(\tau - \tau_{n_l n_m}) \quad (5)$$

where η_{DB} is the proportion of the DB power in the NLoS power, and $\eta_{SB} + \eta_{DB} = 1$, L is the number of the species of the first-bounce scatterers, M is the number of the species of second-bounce scatterers, and $L = M = 4$. As we just consider part of DB paths, it's indispensable to select the (l, m) combinations which are shown in Table II. Here N_l and N_m are the number of first- and second-bounce scatterers, respectively, and $\tau_{n_l n_m} = d_{n_l n_m}/c$ is the delay of path $Tx-S_l-S_m-Rx$. The distance of each path $d_{n_l n_m}$ can also be seen as the superposition of the length of the segments with Tx/Rx, S_l , and S_m as endpoints, i.e.,

$$d_{n_l n_m} = \sqrt{(x_l + D/2)^2 + y_l^2 + z_l^2} + \sqrt{(x_m - D/2)^2 + y_m^2 + z_m^2}. \quad (6)$$

For scatterer S_1 , its location is

$$\begin{cases} x_1 = -D/2 + R_t \cos \beta_t^{n_1} \cos \alpha_t^{n_1} \\ y_1 = R_t \cos \beta_t^{n_1} \sin \alpha_t^{n_1} \\ z_1 = R_t \sin \beta_t^{n_1}. \end{cases} \quad (7)$$

Similarly, the location of S_2 is

$$\begin{cases} x_2 = D/2 - R_r \cos(-\beta_r^{n_2}) \cos(-\alpha_r^{n_2}) \\ y_2 = R_r \cos(-\beta_r^{n_2}) \sin(-\alpha_r^{n_2}) \\ z_2 = R_r \sin(-\beta_r^{n_2}). \end{cases} \quad (8)$$

For the scatterer S_3 , its projection on the xoy plane can be seen as the intersection of the ellipse and the radial, which are the projections of the elliptical cylinder and the segment S_3 -Tx on the xoy plane, respectively, i.e.,

$$\begin{cases} y_3 = \tan(\pi + \alpha_r^{n_3})(x_3 - D/2) \\ \frac{x_3^2}{a^2} + \frac{y_3^2}{a^2 - (D/2)^2} = 1. \end{cases} \quad (9)$$

The complete coordinate of S_3 can be calculated in accordance with the equation of the line S_3 -Rx in 3D case,

$$\begin{aligned} \frac{y_3}{\cos(-\beta_r^{n_3}) \sin(-\alpha_r^{n_3})} &= \frac{z_3}{\sin(-\beta_r^{n_3})} \\ &= \frac{x_3 - D/2}{-\cos(-\beta_r^{n_3}) \cos(-\alpha_r^{n_3})}. \end{aligned} \quad (10)$$

The z coordinate of the scatterer S_4 is fixed, equal to the vertical distance between the top surface and the xoy plane. According to the angle information, we can calculate the coordinate of scatterer S_4 as

$$\begin{cases} x_4 = \frac{z_4}{\sin(-\beta_r^{n_4}) \cos(-\alpha_r^{n_4}) \cos(-\beta_r^{n_4})} + D/2 \\ y_4 = \frac{z_4}{\sin(-\beta_r^{n_4}) \sin(-\alpha_r^{n_4}) \cos(-\beta_r^{n_4})}. \end{cases} \quad (11)$$

B. Simulation model

Based on the reference RS-GBSM, the SoS simulation model is derived. For reference model, infinite scatterers are assumed. While the simulation model is a simplification of the reference model by discretizing the model parameters. We assume that all the phases follow uniform distributions in $[0, 2\pi)$, the EAoAs/AAoAs and EAoDs/AAoDs are all independent and follow the VMF distributions. A VMF distribution is written as

$$f(x) = \frac{e^{k \cos(x-x_0)}}{2\pi I_0(k)} \quad (12)$$

where x_0 is the mean value and k presents the concentration of the VMF distribution. If k is larger, the distribution of x is closer to x_0 , and $I_0(\cdot)$ is the zeroth-order modified Bessel function of the first kind. Therefore, the EAoAs, AAoAs,

EAoDs, AAoDs, and phases of simulation model are a series of discrete values following corresponding VMFs and uniform distribution, respectively.

III. STATISTICAL PROPERTIES

According to the channel models above, some channel characteristics are investigated, including the PDP, CTF, and FCF.

A. PDP

The PDP can be written as a square of the CIR, i.e.,

$$\begin{aligned}\phi(\tau) &= |h(\tau)|^2 \\ &= |h_{\text{LoS}}(\tau)|^2 + |h_{\text{SB}}(\tau)|^2 + |h_{\text{DB}}(\tau)|^2.\end{aligned}\quad (13)$$

It depicts how the power distributes along with the time delay.

B. Delay spread

Due to the multipath effect, the time of arrival (ToA) is dispersive in delay domain. The average delay μ_τ and the root mean square (RMS) delay spread σ_τ are calculated to describe the delay dispersion of the THz indoor channels:

$$\mu_\tau = \frac{\sum \tau \phi(\tau)}{\sum \phi(\tau)} \quad (14)$$

$$\sigma_\tau = \sqrt{\frac{\sum (\tau - \mu_\tau)^2 \phi(\tau)}{\sum \phi(\tau)}}. \quad (15)$$

C. CTF

The CTF is the Fourier transform of the CIR and can be written as

$$H(f) = H_{\text{LoS}}(f) + H_{\text{SB}}(f) + H_{\text{DB}}(f) \quad (16)$$

$$H_{\text{LoS}}(f) = \sqrt{\frac{K}{K+1}} e^{-j2\pi f c \tau_{\text{LoS}} - j2\pi f \tau_{\text{LoS}}} \quad (17)$$

$$\begin{aligned}H_{\text{SB}}(f) &= \sqrt{\frac{\eta_{\text{SB}}}{K+1}} \frac{1}{\sqrt{L}} \sum_{l=1}^L \lim_{N_l \rightarrow \infty} \frac{1}{\sqrt{N_l}} \\ &\quad \sum_{n_l=1}^{N_l} e^{j\varphi_{n_l} - j2\pi f c \tau_{n_l} - j2\pi f \tau_{n_l}}\end{aligned}\quad (18)$$

$$\begin{aligned}H_{\text{DB}}(f) &= \sqrt{\frac{\eta_{\text{DB}}}{K+1}} \frac{1}{\sqrt{LM}} \sum_{l=1}^L \sum_{m=1}^M \lim_{N_l \rightarrow \infty} \lim_{N_m \rightarrow \infty} \frac{1}{\sqrt{N_l N_m}} \\ &\quad \sum_{n_l=1}^{N_l} \sum_{n_m=1}^{N_m} e^{j\varphi_{n_l n_m} - j2\pi f c \tau_{n_l n_m} - j2\pi f \tau_{n_l n_m}}.\end{aligned}\quad (19)$$

D. FCF

The normalized FCF is defined as

$$R(\Delta f) = \frac{E[H(f)H^*(f + \Delta f)]}{\sqrt{\text{Var}[H(f)]\text{Var}[H^*(f + \Delta f)]}} \quad (20)$$

where $E[\cdot]$ and $\text{Var}[\cdot]$ are the calculations of the expectation and variance, respectively.

$H_{\text{SB}}(f)$ and $H_{\text{DB}}(f)$ are independent random processes, then

$$R(\Delta f) = R_{\text{LoS}}(\Delta f) + R_{\text{SB}}(\Delta f) + R_{\text{DB}}(\Delta f). \quad (21)$$

Specifically,

$$R_{\text{LoS}}(\Delta f) = \frac{K}{K+1} e^{j2\pi \Delta f \tau_{\text{LoS}}} \quad (22)$$

$$\begin{aligned}R_{\text{SB}}(\Delta f) &= \frac{\eta_{\text{SB}}}{K+1} \frac{1}{\sqrt{L}} \sum_{l=1}^L E[e^{j2\pi \Delta f \tau_{n_l}}] \\ &= \frac{\eta_{\text{SB}}}{K+1} \frac{1}{\sqrt{L}} \sum_{l=1}^L \int_{-\pi}^{\pi} \int_{-\pi}^{\pi} e^{j2\pi \Delta f \tau_{n_l}} \\ &\quad \times f(\alpha_r^{n_l}) f(\beta_r^{n_l}) d\alpha_r^{n_l} d\beta_r^{n_l}\end{aligned}\quad (23)$$

$$\begin{aligned}R_{\text{DB}}(\Delta f) &= \frac{\eta_{\text{DB}}}{K+1} \frac{1}{\sqrt{LM}} \sum_{l=1}^L \sum_{m=1}^M E[e^{j2\pi \Delta f \tau_{n_l n_m}}] \\ &= \frac{\eta_{\text{DB}}}{K+1} \frac{1}{\sqrt{LM}} \sum_{l=1}^L \sum_{m=1}^M \int_{-\pi}^{\pi} \int_{-\pi}^{\pi} \int_{-\pi}^{\pi} \int_{-\pi}^{\pi} \\ &\quad e^{j2\pi \Delta f \tau_{n_l n_m}} f(\alpha_t^{n_l}) f(\beta_t^{n_l}) f(\alpha_r^{n_m}) \\ &\quad \times f(\beta_r^{n_m}) d\alpha_t^{n_l} d\beta_t^{n_l} d\alpha_r^{n_m} d\beta_r^{n_m}.\end{aligned}\quad (24)$$

Here, $f(\alpha_t^{n_l})$ and $f(\alpha_r^{n_m})$ are the PDFs of the AAoD and EAoA, respectively, $f(\beta_t^{n_l})$ and $f(\beta_r^{n_m})$ are the PDFs of the EAoD and EAoA, respectively.

IV. RESULTS AND ANALYSIS

In this section, we analyze the statistical properties of the proposed 3D GBSMs for THz indoor scenarios, including the PDP, CTF, and FCF. The values of the parameters are set as follows: $a = 2$ m, $D = 1.8$ m, $R_t = R_r = 0.5$ m, $z_4 = 2$ m, $\eta_{\text{SB}} = 0.8$, $\eta_{\text{DB}} = 0.2$, and $N_1 = 40$, $N_2 = 30$, $N_3 = N_4 = 10$ for SB scatterers, while $N_1 = N_2 = 20$, $N_3 = N_4 = 10$ for DB scatterers.

The simulated PDP is shown in Fig. 2. Here, we assume the Ricean factor to be $K = 2$ and the parameters of each scatterer's distribution can be flexibly changed to fit the measurement data. As only the small-scale fading is considered in our proposed model, the level of the simulated PDP is adjusted to compare with the measurement for convenience. We can observe that the simulated result can match the measurement data [28].

According to the PDP, the delay spreads of the channels are analyzed. To compare with the measurement data in [26], the parameters are adjusted as $K = 1.5$ and $D = 2.4$ m

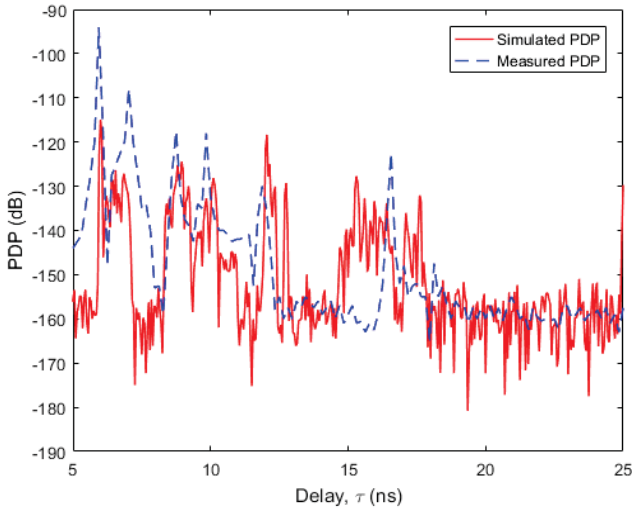


Fig. 2. Comparison of the simulated and measured PDPs.

and the parameters of each scatterer's distribution are also correspondingly amended. The simulated and measured results of average delay and the RMS delay spread of the LoS, SB, and DB components are shown in Table III. The simulated and measured results can fit well.

Fig. 3(a) illustrates the measured CTF, simulated CTF with top surface, and simulated CTF without top surface of the THz indoor channels [26]. Fig. 3(b) shows the details of partial CTF. The parameter setting is the same as that of delay spread simulation, except that we adjust the level of the simulated CTF according to the measurement data. We can see that the fluctuations of three curves are similar, which validates the feasibility of our proposed model. In more details, the fluctuation and the level of the simulated CTF with top surface are closer to the measurement data compared to the simulated CTF without top surface. It indicates a better match between the simulated CTF with top surface and the measured CTF. Therefore, the addition of the top surface is rewarding.

In Fig. 4, we demonstrate the comparison of FCFs among reference model, simulation model, and simulation result. We do the $xcorr()$ operation directly to the CTFs to get the simulation result. All the numbers of scatterers are chosen to be equal to 50, $N_1 = N_2 = N_3 = N_4 = 50$. The trend of three curves are coincident, converging to the FCF of the LoS path $R_{LoS}(\Delta f)$, which is determined along with the frequency interval Δf .

V. CONCLUSIONS

In this paper, we have proposed a 3D RS-GBSM for indoor THz channels. To the best of our knowledge, it is the first time to apply the 3D RS-GBSM to indoor THz channels. Based on the proposed model, the CTF has been derived and some channel characteristics, such as PDP, delay spread, and FCF, have been further investigated. The simulated and measured PDPs and CTFs match well and the significance of the top surface has been proved. The FCFs of reference

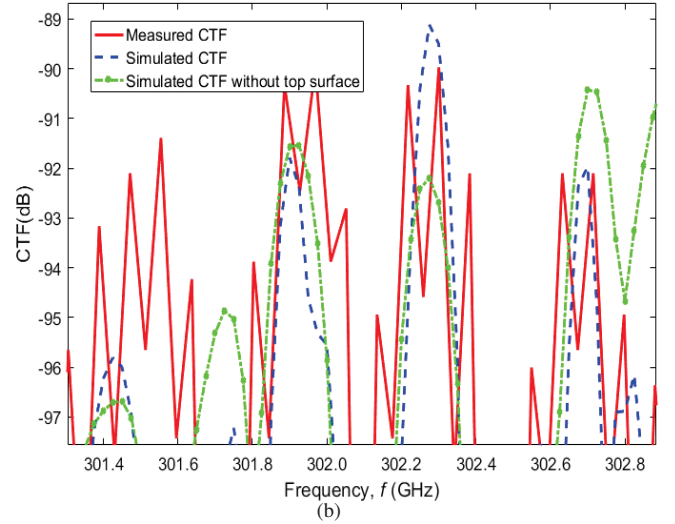
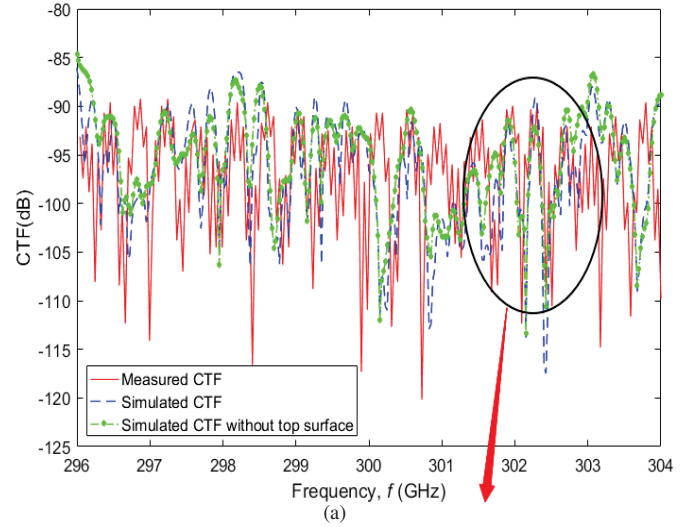


Fig. 3. Comparison of the simulated and measured CTFs.

model, simulation model, and simulation result follow the same trend. The results have shown that the proposed model is valid to depict THz indoor channels. This model can conduce to the designing, performance evaluation, optimization, and deployment of future THz communication systems.

ACKNOWLEDGMENT

This work was supported by the National Key R&D Program of China (No. 2018YFB1801101), National Natural Science Foundation of China (No. 61960206006 and 61771293), Fundamental Research Funds for the Central Universities (No. 2242019R30001 and 2242019R20002), National Postdoctoral Program for Innovative Talents (No. BX20180062), Key Research and Development Program of Shandong Province (2016GGX101014), Fundamental Research Funds of Shandong University (2017JC029), Taishan Scholar Program of

TABLE III
DELAY SPREADS OF LOS, SB, AND DB COMPONENTS.

Component Parameter	LoS		LoS+SB		LoS+SB+DB	
	Simulated	Measured	Simulated	Measured	Simulated	Measured
μ_τ (ns)	8.00	/	18.18	/	20.48	/
σ_τ (ns)	0	0.27	2.85	2.88	3.53	3.49

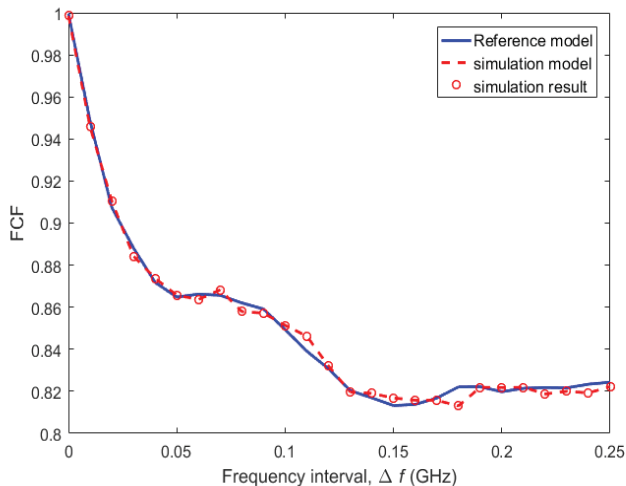


Fig. 4. Comparison of FCFs of the reference model, simulation model, and simulation result.

Shandong Province, and EU H2020 RISE TESTBED Project (734325).

REFERENCES

- [1] H. Elayan, O. Amin, R. M. Shubair, and M. Alouini, "Terahertz communication: The opportunities of wireless technology beyond 5G," in *Proc. CommNet'18*, Marrakech, Morocco, Apr. 2018, pp. 1–5.
- [2] J. Huang, C.-X. Wang, R. Feng, J. Sun, W. Zhang, and Y. Yang, "Multi-frequency mmWave massive MIMO channel measurements and characterization for 5G wireless communication systems," *IEEE J. Sel. Areas Commun.*, vol. 35, no. 7, pp. 1591–1605, July 2017.
- [3] R. Feng, J. Huang, J. Sun, and C.-X. Wang, "A novel 3D frequency domain SAGE algorithm with applications to parameter estimation in mmWave massive MIMO indoor channels," *Sci. China Inf. Sci.*, vol. 60, no. 8, Aug. 2017.
- [4] J. Huang, Y. Liu, C.-X. Wang, J. Sun, and H. Xiao, "5G millimeter wave channel sounders, measurements, and models: Recent developments and future challenges," *IEEE Commun. Mag.*, vol. 57, no. 1, pp. 138–145, Jan. 2019.
- [5] C.-X. Wang, F. Haider, X. Gao, X.-H. You, Y. Yang, D. Yuan, H. Aggoune, H. Haas, S. Fletcher, and E. Hepsaydir, "Cellular architecture and key technologies for 5G wireless communication networks," *IEEE Commun. Mag.*, vol. 52, no. 2, pp. 122–130, Feb. 2014.
- [6] T. Nagatsuma, "Terahertz communications: Past, present and future," in *Proc. IRMMW-THz'15*, Hong Kong, China, Aug. 2015, pp. 1–2.
- [7] I. Seto, K. Hiraga, T. Kürner, A. Fricke, B. Peng, S. Rey, M. Yaita, H. Song, A. Kasamatsu, I. Hosako, D. He, K. Guan, H. Ogawa, A. Bo, Z. Zhong, P. Le Bars, and A. Mounir, "Channel modelling document (CMD)," IEEE 802.15.3d, DCN: 15-14-0310-19-003d, Mar. 2016.
- [8] Q. H. Abbasi, H. El Sallabi, N. Chopra, K. Yang, K. A. Qaraqe, and A. Alomainy, "Terahertz channel characterization inside the human skin for nano-scale body-centric networks," *IEEE Trans. Terahertz Sci. Technol.*, vol. 6, no. 3, pp. 427–434, May 2016.
- [9] H. Elayan, R. M. Shubair, J. M. Jornet, and P. Johari, "Terahertz channel model and link budget analysis for intrabody nanoscale communication," *IEEE Trans. Nanobiosci.*, vol. 16, no. 6, pp. 491–503, Sept. 2017.
- [10] D. He, K. Guan, B. Ai, A. Fricke, R. He, Z. Zhong, A. Kasamatsu, I. Hosako, and T. Kürner, "Channel modeling for kiosk downloading communication system at 300 GHz," in *Proc. EuCAP'17*, Paris, France, Mar. 2017, pp. 1331–1335.
- [11] D. He, K. Guan, A. Fricke, B. Ai, R. He, Z. Zhong, et al. "Stochastic channel modeling for kiosk applications in the terahertz band," *IEEE Trans. Terahertz Sci. Technol.*, vol. 7, no. 5, pp. 502–513, Sept. 2017.
- [12] A. Fricke, C. Homann, and T. Kürner, "Time-domain propagation investigations for terahertz intra-device communications," in *Proc. EuCAP'14*, The Hague, Netherlands, Apr. 2014, pp. 1760–1764.
- [13] B. Peng and T. Kürner, "A stochastic channel model for future wireless THz data centers," in *Proc. ISWCS'15*, Brussels, Belgium, Aug. 2015, pp. 741–745.
- [14] S. Kim and A. Zajić, "Statistical characterization of 300-GHz propagation on a desktop," *IEEE Trans. Veh. Technol.*, vol. 64, no. 8, pp. 3330–3338, Aug. 2015.
- [15] S. Kim and A. Zajić, "Statistical modeling of THz scatter channels," in *Proc. EuCAP'15*, Lisbon, Portugal, Apr. 2015, pp. 1–5.
- [16] S. Priebe and T. Kürner, "Stochastic modeling of THz indoor radio channels," *IEEE Trans. Wireless Commun.*, vol. 12, no. 9, pp. 4445–4455, Sept. 2013.
- [17] A. Moldovan, M. A. Ruder, I. F. Akyildiz, and W. H. Gerstacker, "LOS and NLOS channel modeling for terahertz wireless communication with scattered rays," in *Proc. GC Wkshps'14*, Austin, TX, Dec. 2014, pp. 388–392.
- [18] S. Priebe, C. Jastrow, M. Jacob, T. Kleine-Ostmann, T. Schrader, and T. Kürner, "Channel and propagation measurements at 300 GHz," *IEEE Trans. Antennas Propag.*, vol. 59, no. 5, pp. 1688–1698, May 2011.
- [19] N. Khalid and O. B. Akan, "Wideband THz communication channel measurements for 5G indoor wireless networks," in *Proc. ICC'16*, Kuala Lumpur, Malaysia, Jul. 2016, pp. 1–6.
- [20] M. Salhi, T. Kleine-Ostmann, T. Schrader, M. Kannicht, S. Priebe, and T. Kürner, "Broadband channel measurements in a typical office environment at frequencies between 50 GHz and 325 GHz," in *Proc. EuMC'13*, Nuremberg, Germany, Dec. 2013, pp. 175–178.
- [21] S. Wu, C.-X. Wang, H. Aggoune, M. M. Alwakeel, and X. You, "A general 3D non-stationary 5G wireless channel model," *IEEE Trans. Commun.*, vol. 66, no. 7, pp. 3065–3078, July 2018.
- [22] C.-X. Wang, J. Bian, J. Sun, W. Zhang, and M. Zhang, "A survey of 5G channel measurements and models," *IEEE Commun. Surveys Tuts.*, vol. 20, no. 4, pp. 3142–3168, 4th Quart., 2018.
- [23] A. Al-Kinani, C.-X. Wang, L. Zhou, and W. Zhang, "Channel measurements and models for optical wireless communications: A survey," *IEEE Commun. Surveys Tuts.*, vol. 20, no. 3, pp. 1939–1962, 3rd Quart., 2018.
- [24] Y. Liu, C.-X. Wang, J. Huang, J. Sun, and W. Zhang, "Novel 3-D nonstationary mmWave massive MIMO channel models for 5G high-speed train wireless communications," *IEEE Trans. Veh. Technol.*, vol. 68, no. 3, pp. 2077–2086, Mar. 2019.
- [25] J. Huang, C.-X. Wang, Y. Liu, J. Sun, and W. Zhang, "A novel 3D GBMSM for mmWave MIMO channels," *Sci. China Inf. Sci.*, vol. 61, no. 10, Oct. 2018.
- [26] S. Priebe, M. Kannicht, M. Jacob, and T. Kürner, "Ultra broadband indoor channel measurements and calibrated ray tracing propagation modeling at THz frequencies," *J. Commun. Networks*, vol. 15, no. 6, pp. 547–558, Dec. 2013.
- [27] Y. Yuan, C. Wang, X. Cheng, B. Ai, and D. I. Laurenson, "Novel 3D geometry-based stochastic models for non-isotropic MIMO vehicle-to-vehicle channels," *IEEE Trans. Wireless Commun.*, vol. 13, no. 1, pp. 298–309, Jan. 2014.
- [28] S. Priebe, M. Jacob, C. Jastrow, T. Kleine-Ostmann, T. Schrader, and T. Kürner, "A comparison of indoor channel measurements and ray tracing simulations at 300 GHz," in *Proc. ICIMW'10*, Rome, Italy, Sept. 2010, pp. 1–2.